Nano Res (2009) 2: 327–335
DOI 10.1007/s12274-009-9030-y
Research Article

Vacancy Ordering and Lithium Insertion in III_2VI_3 Nanowires

Hailin Peng[1], Xiao Feng Zhang[2], Ray D. Twesten[3], and Yi Cui[1] (✉)

[1] Department of Materials Science and Engineering, Stanford University, Stanford, California 94305, USA
[2] Electron Microscope Division, Hitachi High Technologies America, Inc., 5100 Franklin Drive, Pleasanton, California 94588, USA
[3] Gatan Inc., 5933 Coronado Lane, Pleasanton, California 94588, USA

Received: 10 January 2009 / Revised: 11 February 2009 / Accepted: 11 February 2009

ABSTRACT

Superlattice structures resulting from vacancy ordering have been observed in many materials. Here we report vacancy ordering behavior in III_2VI_3 nanowires. The formation of layer-like structural vacancies has been achieved during the synthesis of In_2Se_3 nanowires through a vapor-transport route. Doping In_2Se_3 nanowires with small amounts of Ga during synthesis can completely change the structural vacancy ordering from a layer-like to a screw-like pattern for $(In_xGa_{1-x})_2Se_3$ nanowires. Lithium atoms can fill in the layer-like structural vacancies of In_2Se_3 nanowires and generate new types of vacancy and lithium atom ordering superlattices. The screw-patterned vacancies of $(In_xGa_{1-x})_2Se_3$ nanowires show reversible lithium insertion. Our results contribute to the understanding of structure–property correlations of III_2VI_3 materials used in lithium ion storage, photovoltaics, and phase change memory.

KEYWORDS

Nanowire (NW), vacancy ordering, superlattice, III–VI, lithium insertion

Vacancies are a classical point defect and play an important role in atomic diffusion, doping, and color centers in ionic crystals. Vacancy ordering phenomena have been investigated in nonstoichiometric bulk materials including oxides [1–3], chalcogenides [4–6], carbides [7, 8], silicides [9], and nitrides [10]. The ability to arrange vacancies is important for gaining control over material properties. For example, oxygen vacancy ordering in transition metal oxides has been shown to affect their ferroelectric properties and high-temperature superconductivity [11, 12]; intercalation materials such as Li_xTiS_2, Li_xTaS_2, and Li_xCoO_2 have been shown to form superlattice structures upon Li deintercalation, which is due to lithium and vacancy ordering and is critical to the structure stability and kinetics of Li-ion battery electrodes [13–16]; the ordered vacancy compound at the $CuIn(Ga)Se_2$–CdS interface has different electrical properties from $CuIn(Ga)Se_2$ and is believed to play an important role in the high efficiency of $CuIn(Ga)Se_2$ solar cells [5, 17, 18].

The III–VI semiconductors have attracted attention because of their unique structural, optical, and electrical properties, which result in applications including lithium ion batteries [19, 20], photovoltaics [21–23], and phase-change memory [24, 25]. Owing to the mismatch between III and VI atoms, bulk III–VI compounds show a variety of crystal polymorphism

Address correspondence to yicui@stanford. edu

depending on the growth conditions. We and others have recently developed the synthesis of single crystalline In_2Se_3 [26, 27] and GaSe [28] nanowires (NWs) because NW morphology not only provides the opportunity to engineer materials for better device performance in applications such as transistors [29–31], solar cells [32–33], nanogenerators [34], batteries [35–37], and memory devices [38–40], but also affords well-defined nanoscale domains in which to correlate structure and properties [41, 42]. We have observed a metal-to-insulator transition in In_2Se_3 NWs, which correlated with a four-fold superlattice-to-normal-lattice transition induced by additional In vacancies, using single NW electron transport and transmission electron microscopy (TEM) [26]. Herein, we study the vacancy ordering and lithium insertion behaviors in III_2VI_3 NWs. There are two types of ordering of intrinsic structural vacancies in III_2VI_3 NWs: layer-like and screw-like vacancy ordering. Doping In_2Se_3 with small amounts of Ga during NW synthesis can completely change the structural vacancy ordering from layer-like to screw-like. Lithium atoms can easily fill in structural vacancies in layered In_2Se_3 NWs and generate new types of vacancy and lithium ordering superlattices. The screw-like ordered vacancies in $(In_xGa_{1-x})_2Se_3$ NWs can be reversibly filled by lithium atoms.

Crystal structures of III_2VI_3 bulk compounds are commonly defect wurtzite or zinc blende structures with highly ordered vacancies, where every atom is located at the wurtzite or zinc blende sites and one third of the cation sites are occupied by the structural vacancies. Figure 1 shows the structure models and chemical transformations of III_2VI_3 compounds. A virtual III_3VI_3 has a wurtzite structure with tetrahedral covalent bonding between III and VI atoms (Fig. 1(a)). When 1/3 of the group III cation sites are vacant, vacancies can self-organize to form ordered vacancy structures. One way is to create one vacancy plane along the *ab*-direction for every three III-planes (Fig. 1(b)). The resulting III_2VI_3 material has a hexagonal layered structure (α phase) with space group $P6_3$, which has tetrahedral covalent bonding between III and VI atoms within layers of VI–III–VI–III–VI. Layers are linked by van der Waals bonding [42, 43]. The other way is that the structural vacancies on 1/3 of

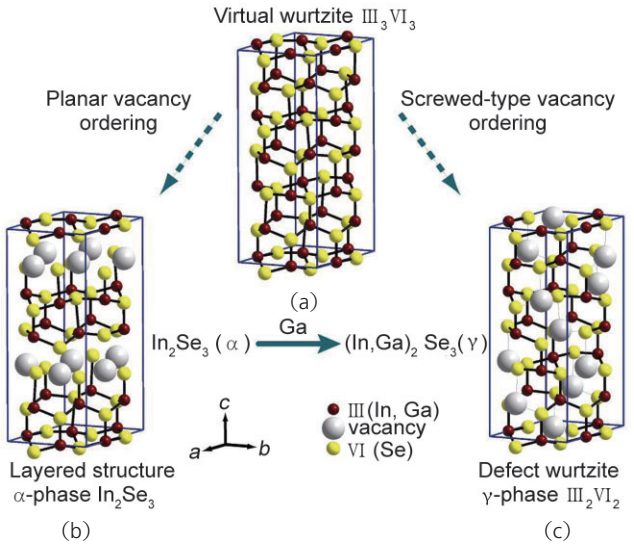

Figure 1 Structure models and chemical transformations of vacancy ordered III–VI compounds: (a) virtual III_3VI_3 with a wurtzite structure; (b) hexagonal layered structure (α phase) of III_2VI_3 with planar cationic vacancy ordering; (c) distorted wurtzite-like structure (γ phase) III_2VI_3 with screw-type cationic vacancy ordering

the cation sites can produce a screw pattern along the *c*-axis. Consequently, the III_2VI_3 compound forms a distorted wurtzite structure (γ phase) with space group $P6_1$ or $P6_5$ (Fig. 1(c)), denoted as a vacancy-ordered-in-screw-form (VOSF) phase [43, 44]. In fact, the VOSF phase in $(Ga_xIn_{1-x})_2Se_3$ compound is stable within a wide composition range of x from 0.03 to 0.70 [45].

We synthesized single-crystalline III_2VI_3 NWs by a vapor transport and deposition method, using different powders as the source materials. Single-crystalline In_2Se_3 NWs were grown inside a 12-inch horizontal tube furnace using the Au nanoparticle-catalyzed vapor–liquid–solid (VLS) growth method reported previously [26, 28]. For $(In_xGa_{1-x})_2Se_3$ NW growth, In_2Se_3 powder and small amount of additional GaSe powder were placed into the center of the tube furnace, where the temperature was 700 °C. A carrier gas (2% H_2 and 98% N_2) transported the vapor of GaSe and In_2Se_3 precursors downstream, and $(In_xGa_{1-x})_2Se_3$ NWs were grown on a Si ⟨100⟩ substrate with 20 nm diameter Au nanoparticles, at a temperature of approximately 620 °C. Typical synthesis conditions for $(In_xGa_{1-x})_2Se_3$ are pressure = 25 Torr, growth time = 1–5 h, and gas flow = 100 sccm (standard

cubic centimeters per minute). The NWs were characterized using an FEI Sirion scanning electron microscope (SEM), a PANalytical X'Pert PRO X-ray diffraction (XRD) system, Hitachi 300 kV H-9500 and Philips CM20 TEM, and an energy dispersive X-ray spectrometer (EDS) fitted to one TEM. Electron energy loss spectroscopy (EELS) data were acquired using a Gatan Model 776 Enfina spectrometer coupled to a Hitachi HD2300 scanning transmission electron microscope (STEM) operating at 200 keV.

Representative SEM images in Figs. 2(a) and 2(b) show high density growth of In_2Se_3 and $(In_xGa_{1-x})_2Se_3$ NWs on a Si ⟨100⟩ substrate, respectively. The NW diameters range from 30 to 300 nm and the lengths are up to tens of microns. High-resolution SEM studies indicate that a nanoparticle is observed at the end of each NW, suggesting a VLS growth assisted by the Au nanoparticle catalyst.

Powder XRD was used to confirm the structure conversion during the III_2VI_3 NW growth. In_2Se_3 NWs were the sole product using In_2Se_3 powder as the source material. Figure 2(c) shows a typical powder XRD pattern of In_2Se_3 NWs and its reference diffractogram (α phase, $P6_3$, $a=b=0.4025$ nm and $c=1.9235$ nm, ICDD card #00-034-1279) for comparison. The phase identity of the NWs was confirmed to be layered In_2Se_3 with space group $P6_3$. When the additional GaSe powder precursor was used, the as-grown NWs were confirmed to be $(In_xGa_{1-x})_2Se_3$ (γ phase, $P6_1$, ICDD card #01-087-1482), as shown in Fig. 2(d). The additional peak at 33° marked by a star symbol comes from the ⟨200⟩ plane of the Si substrate. No other $(In_xGa_{1-x})_2Se_3$ phases or other crystalline impurity phases, such as In_2Se_3 (Fig. 2(c)) are detectable by powder XRD, which highlights the rational control of the III_2VI_3 phase afforded by the vapor-transport method.

The results of structure and composition characterization of In_2Se_3 NWs with layer-ordered vacancies have been reported in previous publications [26, 42]. To characterize the microstructures and chemical compositions of the as-grown $(In_xGa_{1-x})_2Se_3$ NWs, we have carried out EDS, high-resolution TEM (HRTEM), and electron diffraction (ED) studies. Figure 3(a) shows a low-magnification TEM image of a zigzag $(In_xGa_{1-x})_2Se_3$ NW with a nanoparticle at the tip. The diameter of the NW is about 65 nm and the length extends up to several microns. The catalyst particle at the tip has a diameter of 60–70 nm. EDS spectra of the catalyst particle indicate the presence of both Au and In, implying Au–In alloy formation (Fig. 3(c)). EDS analyses reveal that the NW has the composition $(In_{0.84}Ga_{0.16})_2Se_3$ with a Ga/In atomic ratio of ~0.16. The HRTEM image (Fig. 3(b)) of the same NW reveals sequentially bright/dark contrast fringes throughout the entire length of the wires, which run parallel to the NW–Au particle interface with an angle of ~57° to the NW long axis. The HRTEM image (Fig. 3(d)) further reveals the periodic spacing

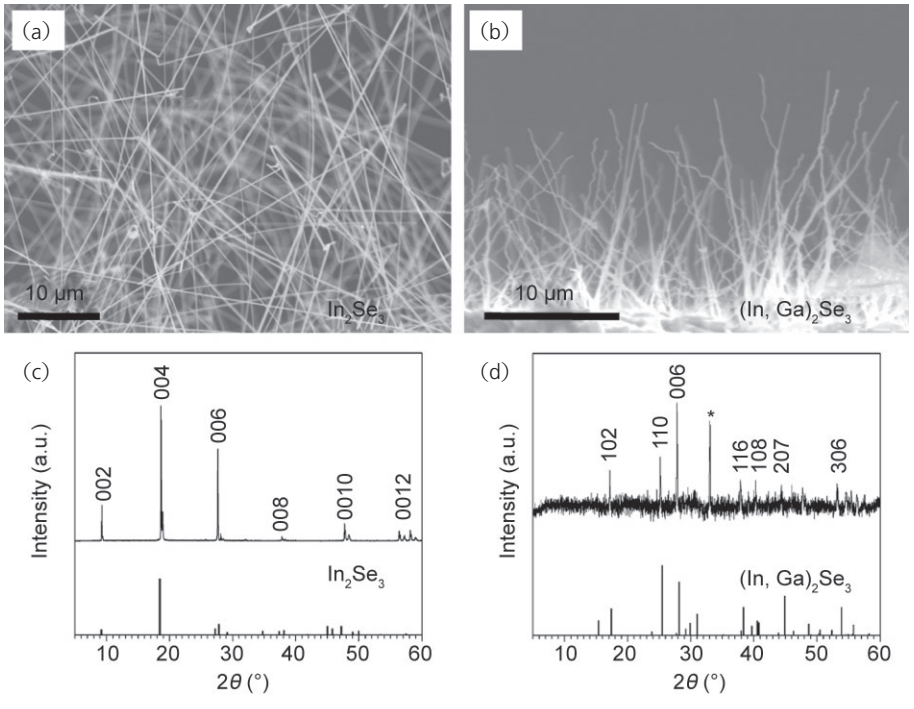

Figure 2 Typical SEM images of (a) In_2Se_3 and (b) $(In_xGa_{1-x})_2Se_3$ NWs grown on Si ⟨100⟩ substrates,. The corresponding powder XRD patterns of (c) In_2Se_3 and (d) $(In_xGa_{1-x})_2Se_3$ NWs on the Si ⟨100⟩ substrates with reference diffractograms (ICDD cards #00-034-1279 and 01-087-1482, respectively). The peak at 33° marked by the star symbol comes from the ⟨200⟩ plane of the Si substrate

of these fringes is ~1.92 nm, as marked in the image, corresponding to the (001) planes of $(In_{0.84}Ga_{0.16})_2Se_3$. In order to determine the vacancy ordering and atomic displacement in $(In_{0.84}Ga_{0.16})_2Se_3$ NWs, atomic-resolution TEM observation and electron diffraction were carried out along different zone axes. Figure 3(e) shows a lattice-resolved TEM image taken along the [010] direction. The unit cell marked × the yellow box has a dimension of 0.612 nm by 1.92 nm, corresponding to the lattice spacing of (100) and (006) planes of γ-$(In_xGa_{1-x})_2Se_3$, respectively. The white spot arrays correspond to the ordered structural vacancies [44]. The obvious contrast difference in white spots reveals the displacements of two-coordinate Se atoms around the vacancies, which has been previously observed in $(In_xGa_{1-x})_2Se_3$ thin films [44]. Figures 3(f) and 3(g) show a selected area electron diffraction (SAED) pattern of the NWs and a simulation of the diffraction pattern based on the vacancy ordered screw structure model (Fig. 1(c)), respectively. They were both taken along the [010] zone axis. The observed diffraction spots and intensity distribution of the SAED pattern matche well with the simulated pattern, further confirming the screw vacancy ordering structure in the $(In_xGa_{1-x})_2Se_3$ NW. The diffraction spots are indexed in the hexagonal system with $a = 0.707$ nm and $c = 1.92$ nm. Note that the lattice constants of single crystals of γ-$(In_xGa_{1-x})_2Se_3$ were found to depend on the Ga content [46]. At $x = 0.84$, the lattice constants are $a = \sim 0.706$ nm, $c = \sim 1.920$ nm [46], consistent with our TEM and ED observations of as-grown $(In_{0.84}Ga_{0.16})_2Se_3$ NWs.

Since the ordering of vacancies and lithium has a significant effect on the physical properties of the host

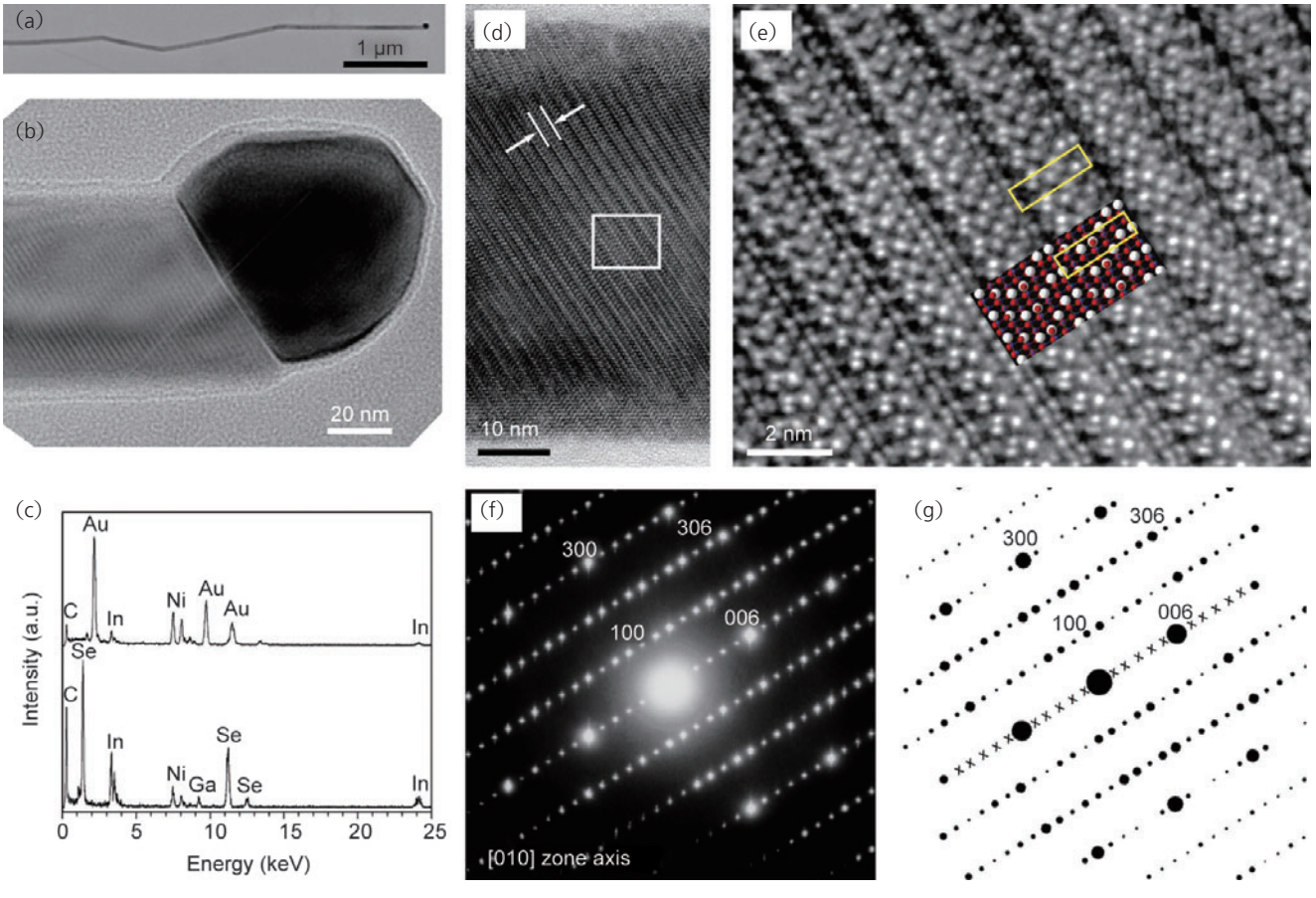

Figure 3 (a) Low-magnification TEM image of a single-crystalline $(In_xGa_{1-x})_2Se_3$ NW with a nanoparticle at the tip. (b) Enlarged TEM image of the end of the same $(In_xGa_{1-x})_2Se_3$ NW. (c) EDS spectra of the same $(In_xGa_{1-x})_2Se_3$ NW (bottom) and the tip (top). The Ni and C peaks come from the Ni grid. (d) High-magnification TEM image of the $(In_xGa_{1-x})_2Se_3$ NW showing sequentially bright/dark contrast fringes. (e) HRTEM image recorded from the area indicated by the white box in (d) and the atomic arrangements of $(In_xGa_{1-x})_2Se_3$ along the [010] zone axis. (f) The corresponding SAED pattern. (g) Simulated diffraction pattern of γ-$(In_xGa_{1-x})_2Se_3$ using a MacTempas program

materials and its electrochemical applications in Li batteries [47, 48], we studied Li insertion in In_2Se_3 and $(In_xGa_{1-x})_2Se_3$ nanostructures using EELs, TEM, and ED techniques. Lithium has very small atomic size and can penetrate into most materials. Li insertion in In_2Se_3 and $(In_xGa_{1-x})_2Se_3$ NWs was realized by immersing the NWs into *n*-butyllithium (BuLi) dissolved in hexane solution (0.1 mol/L) in an inert atmosphere for 20 h at room temperature followed by extensive washing. We performed EELS in order to characterize the change in chemical composition. The EEL spectra obtained from single In_2Se_3 NWs before (pristine) and after 20 h lithiation ($Li_xIn_2Se_3$) are shown in Fig. 4(a). A peak located at ~56 eV with onset at ~54 eV assigned to the Se 3d core level was observed in the both pristine and lithiated NWs, but a large peak centered around 61 eV with onset at ~58 eV attributed to the Li K-edge structure was observed only in the $Li_xIn_2Se_3$ NWs, indicating the presence of Li in this material.

$Li_xIn_2Se_3$ nanostructures remain crystalline and exhibit good chemical stability in the air. Extensive TEM and ED studies reveal a superlattice transformation upon Li insertion. Figure 4(b) shows a TEM image of $Li_xIn_2Se_3$ nanostructures, which are a mixture of NWs and nanoflakes. The $Li_xIn_2Se_3$ NWs retain the wire morphology and show a uniform contrast, which suggests the spatial homogenization

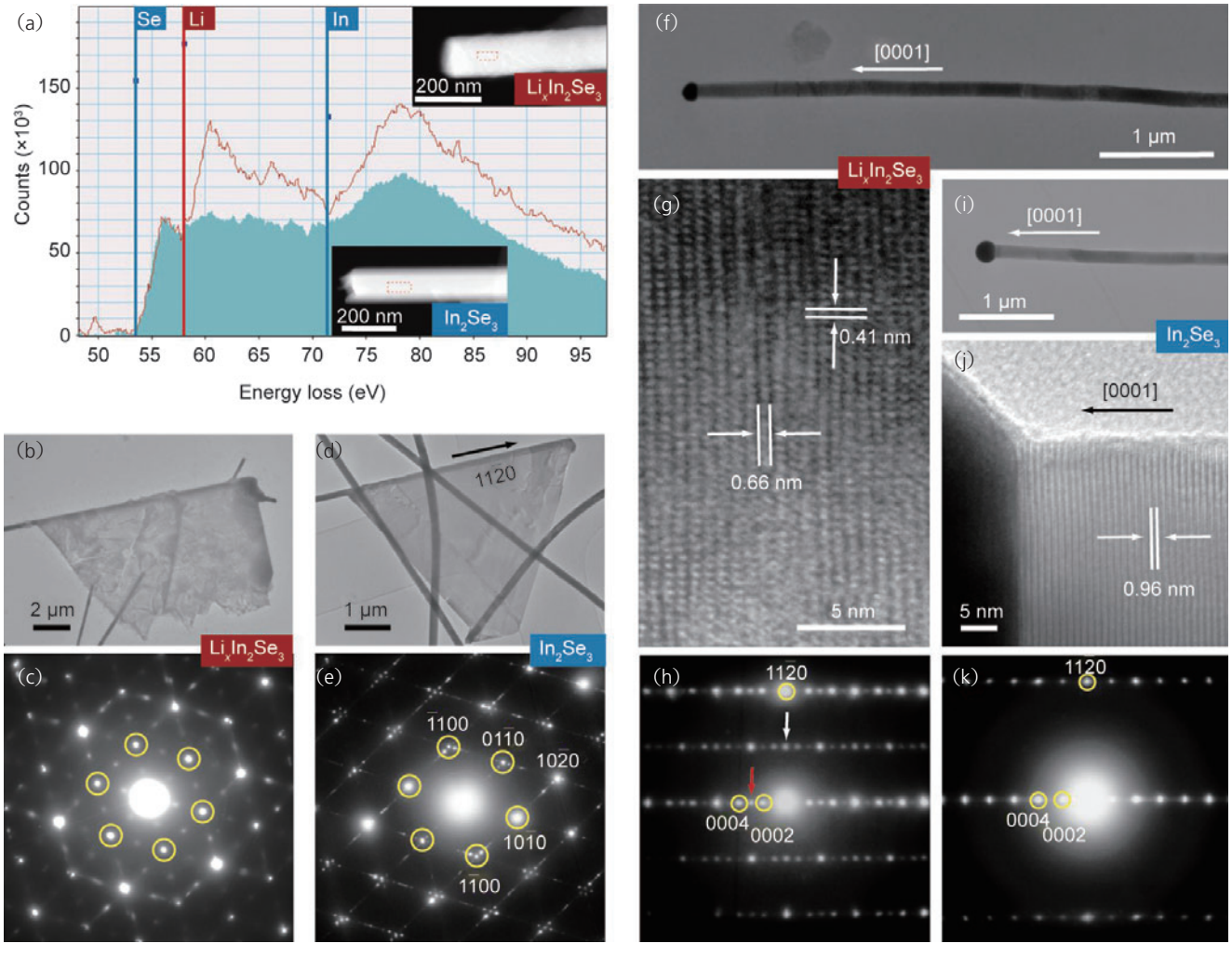

Figure 4 (a) EEL spectra of pristine In_2Se_3 NW (blue) and $Li_xIn_2Se_3$ NW (red). Insets: STEM images of In_2Se_3 NW (bottom) and $Li_xIn_2Se_3$ NW (top). (b) TEM image of $Li_xIn_2Se_3$ NWs and nanoflakes. (c) SAED pattern of the $Li_xIn_2Se_3$ nanoflake. (d) TEM image of pristine In_2Se_3 NWs and nanoflakes. (e) SAED pattern of pristine In_2Se_3 nanoflake taken along the [0001] zone axis. (f), (g) TEM images of a $Li_xIn_2Se_3$ NW with the [0001] direction and (h) SAED pattern. (i), (j) TEM images of a pristine In_2Se_3 NW with the [0001] growth direction and (k) SAED pattern for comparison

of lithium. However, compared to the uniform contrast in the pristine In_2Se_3 nanostructures (Fig. 4(d)) and $Li_xIn_2Se_3$ NWs, the large size $Li_xIn_2Se_3$ nanoflakes exhibit large contrast differences, suggesting that spatial inhomogeneities exist. As shown in Fig. 4(c), the SAED pattern taken along the [0001] zone axis of the $Li_xIn_2Se_3$ nanoflake reveals a diffraction pattern with a hexagonal symmetry, confirming the single-crystal nature. Compared to the typical diffraction pattern of the pristine In_2Se_3 nanoflake taken along the [0001] zone axis (Fig. 4(e)), two different types of diffraction spots can be distinguished in the $Li_xIn_2Se_3$ nanoflake. The main diffraction spots marked by yellow circles in Fig. 4(c) are assigned to the hexagonal In_2Se_3 lattice. New superlattice reflection spots observed in Fig. 4(c) correspond to a unit cell $a=2a_0$, which are different from the four- or eight-fold superlattice reflections commonly found [26] in the pristine In_2Se_3 nanoflake because of the ordering of additional In vacancies (Fig. 4(e)) (Note: the additional In vacancy ordering is different from the structural vacancy ordering). The superlattice transformation reveals the presence of Li insertion and ordering in $Li_xIn_2Se_3$. Similar phenomena were also found in previous work with $Li_xIn_2Se_3$ thin films [19]. This lithium superstructure formed in the $Li_xIn_2Se_3$ thin films when $x=1/4$, which was confirmed by electrochemical potential spectroscopy measurements and TEM studies [19].

To further determine the nature of Li intercalation in the cationic vacancy plane of the layered In_2Se_3 nanostructures, we used TEM to examine the $Li_xIn_2Se_3$ NWs along the *ab*-plane. In_2Se_3 NWs with the [0001] growth direction are convenient for this purpose since their long axis is perpendicular to the *ab*-plane. Figure 4(f) shows a typical TEM image of a [0001] $Li_xIn_2Se_3$ NW with a diameter of about 120 nm and a length up to several microns. The HRTEM image shows lattice fringes of the $Li_xIn_2Se_3$ NW taken along the [1–100] zone axis (Fig. 4(g)). The corresponding SAED pattern confirms the single crystal nature (Fig. 4(h)). For comparison, typical TEM images and the corresponding SAED pattern of a pristine [0001] In_2Se_3 NW taken along the [1–100] zone axis are shown in Figs. 4(i)–(k). The main diffraction spots-marked by yellow circles in Figs. 4(h) and 4(k) correspond to the hexagonal In_2Se_3 lattice, which reveals that the $Li_xIn_2Se_3$ keeps the same layered structure as In_2Se_3 while expanding the lattice spacing. Li intercalant superlattice spots, indicated by the white arrow (Fig. 4(h)), have twice the spacing of the d_{11-20} spacing in real space, which is consistent with the superlattice reflections in the SAED pattern taken along the [0001] zone axis (Fig. 4(c)). The corresponding lattice spacing of ~0.41 nm is also resolved in the HRTEM image (Fig. 4(g)). The presence of another new set of Li intercalant superlattice spots marked by the red arrow (Fig. 4(h)) has a corresponding lattice spacing of ~0.66 nm (Fig. 4(g)), which is two thirds of the d_{0002} spacing. The data suggest that the ordered Li atoms exist in the cationic vacancy plane of the layered In_2Se_3. Determination of the exact position of lithium atoms and vacancies has proved difficult due to the resolution of our TEM (0.2 nm for Philips CM20 TEM) and the instability of the Li intercalant samples under the high-energy transmission electron beam [47], and requires future study.

Interestingly, the γ-$(In_xGa_{1-x})_2Se_3$ NWs with screw-type cationic vacancy ordering show reversible Li insertion in their structural framework. A typical TEM image of a lithiated NW, $Li_x(In_{0.84}Ga_{0.16})_2Se_3$, after 20 h lithiation and with minimum air exposure reveals good structural stability after Li insertion (Fig. 5(a)). Extensive HRTEM and ED studies show that the $Li_x(In_{0.84}Ga_{0.16})_2Se_3$ NWs retain the NW morphology and wurtzite structure while having a slight lattice expansion compared to pristine $(In_{0.84}Ga_{0.16})_2Se_3$ NWs. The lattice spacing is ~0.334 nm, as marked in Fig. 5(b), corresponding to the (006) planes of the $(In_{0.84}Ga_{0.16})_2Se_3$ NW with ~4.6% lattice expansion. The corresponding SAED pattern (Fig. 5(b) inset) confirms the single-crystal nature. Compared to the SAED pattern of the $(In_{0.84}Ga_{0.16})_2Se_3$ NW taken along the same [010] zone axis (Fig. 3(f)), the reflections with weak intensity such as (001) and (100) disappear, leaving only the basic strong reflections such as (006) and (300). This suggests the uniform intercalation of Li in the cationic vacancy sites of $(In_{0.84}Ga_{0.16})_2Se_3$ NWs. Upon exposure to air for several minutes, $(In_{0.84}Ga_{0.16})_2Se_3$ NWs become core-shell NWs as shown in TEM images (Fig. 5(c)). Am HRTEM image of the shell (Fig. 5(c)) reveals lattice

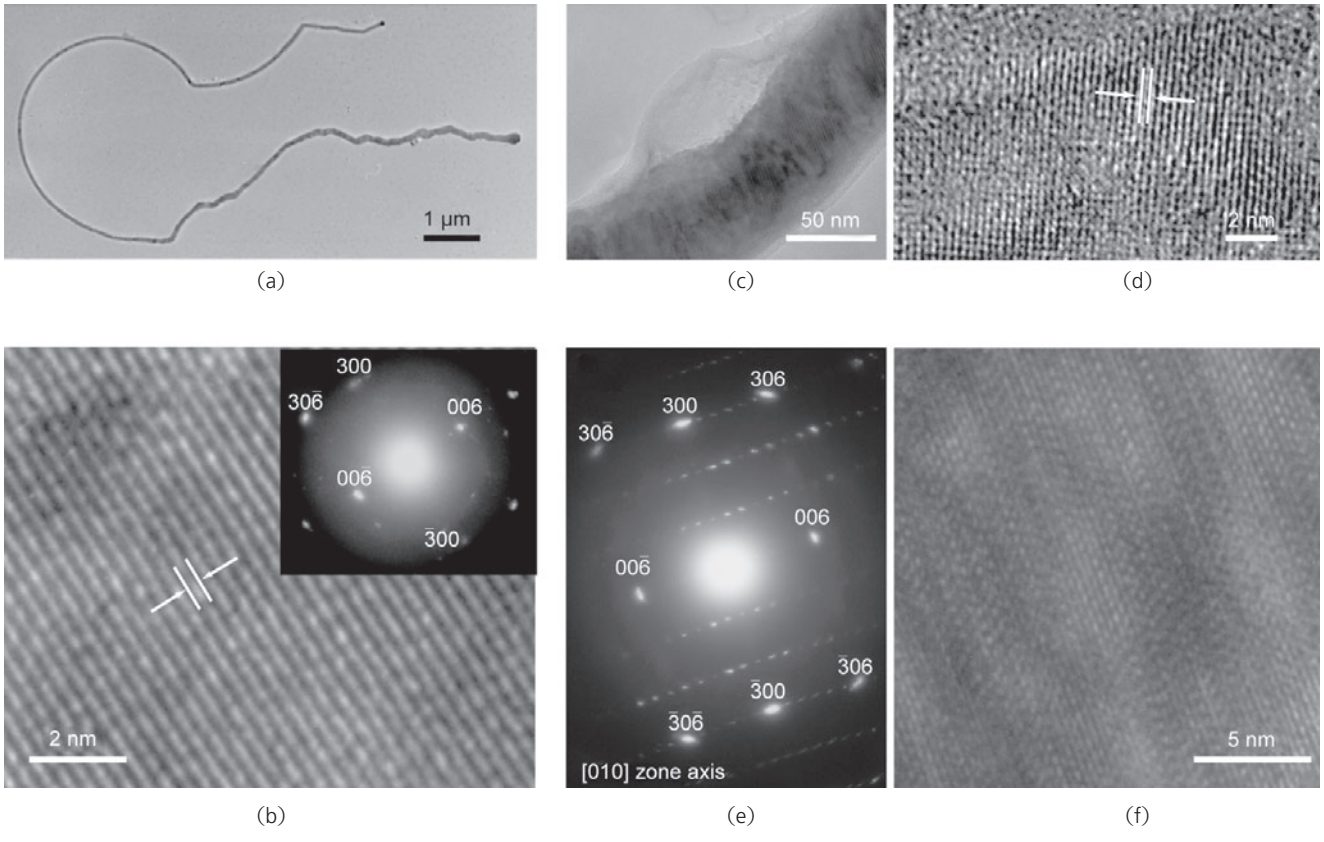

Figure 5 (a) Low magnification TEM image of a $Li_x(In_{0.84}Ga_{0.16})_2Se_3$ NW. (b) HRTEM image of the $Li_x(In_{0.84}Ga_{0.16})_2Se_3$ NW showing lattice fringes. Inset: SAED pattern of the $Li_x(In_{0.84}Ga_{0.16})_2Se_3$ NW taken along the [010] zone axis. (c) Low magnification TEM image of a $Li_x(In_{0.84}Ga_{0.16})_2Se_3$ NW showing the core-shell structure, after exposure in air for several minutes. (d) HRTEM image of the shell. ED pattern (e) and HRTEM image (f) of the core of $Li_x(In_{0.84}Ga_{0.16})_2Se_3$ NW taken along the [010] zone axis, after exposure to air for several minutes

fringe with the typical spacing of 0.270 nm, consistent with the (111) planes of cubic Li_2O. Note that the shell is polycrystalline, and is unstable under the high-energy electron beam irradiation. Interestingly, the structural characters of screw-type vacancy ordering reappear in the NW core, as shown in the SEAD pattern (Fig. 5(e)) and the HRTEM image (Fig. 5(f)), suggesting reversible Li insertion/extraction in $(In_xGa_{1-x})_2Se_3$ NWs.

In summary, structural vacancy ordering and rational conversions in single-crystalline III_2VI_3 NWs have been demonstrated. The arrangement of structural vacancies at the nanoscale is achieved during the synthesis of III_2VI_3 NWs through a vapor-transport route. Superlattice structures and vacancy ordering phenomena in both III_2VI_3 and Li intercalated III_2VI_3 NWs were investigated in detail by HRTEM, coupled with ED and EELS techniques, and the results might provide essential insights into the engineering of future materials for Li storage, solar cells, and phase-change memory.

Acknowledgements

Y. C. acknowledges support from U. S. Department of Energy under the Award Number DE-FG36-08GOI8004. We thank David T. Schoen for helpful discussion.

References

[1] Jia, C. L.; Lentzen, M.; Urban, K. Atomic-resolution imaging of oxygen in perovskite ceramics. *Science* **2003**, *299*, 870–873.

[2] Muller, D. A.; Nakagawa, N.; Ohtomo, A.; Grazul, J. L.; Hwang, H. Y. Atomic-scale imaging of nanoengineered oxygen vacancy profiles in $SrTiO_3$. *Nature* **2004**, *430*, 657–661.

[3] Coey, J. M. D.; Douvalis, A. P.; Fitzgerald, C. B.; Venkatesan, M. Ferromagnetism in Fe-doped SnO_2 thin films. *Appl. Phys. Lett*. **2004**, *84*, 1332–1334.

[4] Dai, Z. R.; Ohuchi, F. S. Vacancy ordering of Ga_2Se_3 at GaSe/GaAs(100) interface. *Appl. Phys. Lett.* **1998**, *73*, 966–968.

[5] Zhang, S. B.; Wei, S. H.; Zunger, A.; Katayama-Yoshida, H. Defect physics of the $CuInSe_2$ chalcopyrite semiconductor. *Phys. Rev. B* **1998**, *57*, 9642–9656.

[6] Teraguchi, N.; Kato, F.; Konagai, M.; Takahashi, K.; Nakamura, Y.; Otsuka, N. Vacancy ordering of Ga_2Se_3 films by molecular-beam epitaxy. *Appl. Phys. Lett.* **1991**, *59*, 567–569.

[7] Rempel, A. A. The effects of atomic and vacancy ordering in nonstoichiometric carbides. *Usp. Fiz. Nauk.* **1996**, *166*, 33–62.

[8] Lipatnikov, V. N.; Lengauer, W.; Ettmayer, P.; Keil, E.; Groboth, G.; Kny, E. Effects of vacancy ordering on structure and properties of vanadium carbide. *J. Alloys Comp.* **1997**, *261*, 192–197.

[9] Lee, T. L.; Chen, L. J.; Chen, F. R. Evolution of vacancy ordering and defect structure in epitaxial YSi_{2-x} thin-films on (111) Si. *J. Appl. Phys.* **1992**, *71*, 3307–3312.

[10] Tian, W. H.; Sano, T.; Nemoto, M. Structure of perovskite carbide and nitride precipitates in L10-ordered TiAl. *Philos. Mag. A* **1993**, *68*, 965–976.

[11] Scott, J. F.; Matthew, D. Oxygen-vacancy ordering as a fatigue mechanism in perovskite ferroelectrics. *Appl. Phys. Lett.* **2000**, *76*, 3801–3803.

[12] Ourmazd, A.; Rentschler, J. A.; Spence, J. C. H.; O'Keeffe, M.; Graham, R. J.; Johnson, D. W.; Rhodes, W. W. Microstructure, oxygen ordering and planar defects in the high-T_c superconductor $YBa_2Cu_3O_{6.9}$.*Nature* **1987**, *327*, 308–310.

[13] Thompson, A. H. Lithium ordering in Li_xTiS_2. *Phys. Rev. Lett.* **1978**, *40*, 1511–1514.

[14] McKinnon, W. R.; Dahn, J. R. Lithium order-disorder transitions in Li_xTaS_2. *Sol. State Comm.* **1983**, *48*, 43–45.

[15] Reimers, J. N.; Dahn, J. R. Electrochemical and *in situ* X-ray-diffraction studies of lithium intercalation in Li_xCoO_2. *J. Electrochem. Soc.* **1992**, *139*, 2091–2097.

[16] Wolverton, C.; Zunger, A. Cation and vacancy ordering in Li_xCoO_2. *Phys. Rev. B* **1998**, *57*, 2242–2252.

[17] Peng, H. L.; Xie, C.; Schoen, D. T.; McIlwrath, K.; Zhang, X. F.; Cui, Y. Ordered vacancy compounds and nanotube formation in $CuInSe_2$–CdS core-shell nanowires. *Nano Lett.* **2007**, *7*, 3734–3738.

[18] Schmid, D., Ruckh, M., Grunwald, F., Schock, H. W. Chalcopyrite/defect chalcopyrite heterojunctions on the basis of $CuInSe_2$. *J. Appl. Phys.* **1993**, *73*, 2902–2909.

[19] Julien, C. M.; Balkanski, M. Lithium reactivity with III-VI layered compounds. *Mater. Sci. Eng. B* **2003**, *100*, 263–270.

[20] Julien, C.; Khelfa, A.; Benramdane, N.; Guesdon, J. P.; Dzwonkowski, P.; Samaras, I.; Balkanski, M. Lithium insertion in indium selenide films—Åpplication to microbatteries. *Mater. Sci. Eng. B* **1994**, *23*, 105–115.

[21] Kwon, S. H.; Ahn, B. T.; Kim, S. K.; Yoon, K. H.; Song, J. Growth of $CuIn_3Se_5$ layer on $CuInSe_2$ films and its effect on the photovoltaic properties of In_2Se_3/$CuInSe_2$ solar cells. *Thin Solid Films* **1998**, *323*, 265–269.

[22] Martine-Pastor, J.; Segura, A.; Valdes, J. L.; Chevy, A. Electrical and photovoltaic properties of indium-tin-oxide para-InSe Au solar-cells. *J. Appl. Phys.* **1987**, *62*, 1477–1483.

[23] Gordillo, G.; Calderon, C. CIS thin film solar cells with evaporated InSe buffer layers. *Sol. Energy Mater. Sol. Cells* **2003**, *77*, 163–173.

[24] Lee, H.; Kim, Y. K.; Kim, D.; Kang, D. H. Switching behavior of indium selenide-based phase-change memory cell. *IEEE Trans. Magn.* **2005**, *41*, 1034–1036.

[25] Gibson, G. A.; Chaiken, A.; Nauka, K.; Yang, C. C.; Davidson, R.; Holden, A.; Bicknell, R.; Yeh, B. S.; Chen, J.; Liao, H.; Subramanian, S.; Schut, D.; Jasinski, J.; Liliental-Weber, Z. Phase-change recording medium that enables ultrahigh-density electron-beam data storage. *Appl. Phys. Lett.* **2005**, *86*, 051902.

[26] Peng, H. L.; Schoen, D. T.; Meister, S.; Zhang, X. F.; Cui, Y. Synthesis and phase transformation of In_2Se_3 and $CuInSe_2$ nanowires. *J. Am. Chem. Soc.* **2007**, *129*, 34–35.

[27] Sun, X. H.; Yu, B.; Ng, G.; Nguyen, T. D.; Meyyappan, M. III-VI compound semiconductor indium selenide (In_2Se_3) nanowires: Synthesis and characterization. *Appl. Phys. Lett.* **2006**, *89*, 233121.

[28] Peng, H. L.; Meister, S.; Chan, C. K.; Zhang, X. F.; Cui, Y. Morphology control of layer-structured gallium selenide nanowires. *Nano Lett.* **2007**, *7*, 199–203.

[29] Huang, Y.; Duan, X. F.; Cui, Y.; Lauhon, L. J.; Kim, K. H.; Lieber, C. M. Logic gates and computation from assembled nanowire building blocks. *Science* **2001**, *294*, 1313–1317.

[30] Goldberger, J.; Hochbaum, A. I.; Fan, R.; Yang, P. D. Silicon vertically integrated nanowire field effect transistors. *Nano Lett.* **2006**, *6*, 973–977.

[31] Thelander, C.; Martensson, T.; Bjork, M. T.; Ohlsson, B. J.; Larsson, M. W.; Wallenberg, L. R.; Samuelson, L. Single-electron transistors in heterostructure nanowires. *Appl. Phys. Lett.* **2003**, *83*, 2052–2054.

[32] Law, M.; Greene, L. E.; Johnson, J. C.; Saykally, R.; Yang, P. D. Nanowire dye-sensitized solar cells. *Nat. Mater.* **2005**, *4*, 455–459.

[33] Tian, B.; Zheng, X.; Kempa, T. J.; Fang, Y.; Yu, N.; Yu, G.; Huang, J.; Lieber, C. M. Coaxial silicon nanowires as solar cells and nanoelectronic power sources. *Nature* **2007**, *449*, 885–889.

[34] Wang, Z. L.; Song, J. H. Piezoelectric nanogenerators based on zinc oxide nanowire arrays. *Science* **2006**, *312*, 242–246.

[35] Chan, C. K.; Peng, H. L.; Liu, G.; McIlwrath, K.; Zhang, X. F.; Huggins, R. A.; Cui, Y. High-performance lithium battery anodes using silicon nanowires. *Nat. Nanotechnol.* **2008**, *3*, 31–35.

[36] Chan, C. K.; Zhang, X. F.; Cui, Y. High capacity Li ion battery anodes using Ge nanowires. *Nano Lett.* **2008**, *8*, 307–309.

[37] Kim, D. K.; Muralidharan, P.; Lee, H. -W.; Ruffo, R.; Yang, Y.; Chan, C. K.; Peng, H.; Huggins, R. A.; Cui, Y. Spinel $LiMn_2O_4$ nanorods as lithium ion battery cathodes. *Nano Lett.* **2008**, *8*, 3948–3952.

[38] Yu, D.; Wu, J.; Gu, Q.; Park, H. Germanium telluride nanowires and nanohelices with memory-switching behavior. *J. Am. Chem. Soc.* **2006**, *128*, 8148–8149.

[39] Jung, Y.; Lee, S. -H.; Ko, D. -K.; Agarwal, R. Synthesis and characterization of $Ge_2Sb_2Te_5$ nanowires with memory switching effect. *J. Am. Chem. Soc.* **2006**, *128*, 14026–14027.

[40] Meister, S.; Peng, H.; McIlwrath, K.; Jarausch, K.; Zhang, X. F.; Cui, Y. Synthesis and characterization of phase-change nanowires. *Nano Lett.* **2006**, *6*, 1514–1517.

[41] Schoen, D. T.; Xie, C.; Cui, Y. Electrical switching and phase transformation in silver selenide nanowires. *J. Am. Chem. Soc.* **2007**, *129*, 4116–4117.

[42] Peng, H. L.; Xie, C.; Schoen, D. T.; Cui, Y. Large anisotropy of electrical properties in layer-structured In_2Se_3 nanowires. *Nano Lett.* **2008**, *8*, 1511–1516.

[43] Ye, J. P.; Soeda, S.; Nakamura, Y.; Nittono, O. Crystal structures and phase transformation in In_2Se_3 compound semiconductor. *Jpn. J. Appl. Phys.* **1998**, *37*, 4264–4271.

[44] Ye, J.; Nakamura, Y.; Nittono, O. Vacancy ordered structure of the III_2VI_3 compound semiconductor $(Ga_xIn_{1-x})_2Se_3$ studied by electron diffraction and microscopy. *Philos. Mag. A* **1996**, *73*, 169–186.

[45] Ye, J. P.; Nakamura, Y.; Nittono, O. Growth of III_2VI_3 compound semiconductor $(Ga_xIn_{1-x})_2Se_3$ single crystals with giant optical activity for visible and infrared light. *J. Appl. Phys.* **2000**, *87*, 933–938.

[46] Ye, J. P.; Yoshida, T.; Nakamura, Y.; Nittono, O. Realization of giant optical rotatory power for red and infrared light using III_2VI_3 compound semiconductor $(Ga_xIn_{1-x})_2Se_3$. *Jpn. J. Appl. Phys.* **1996**, *35*, 4395–4400.

[47] Shao-Horn, Y.; Croguennec, L.; Delmas, C.; Nelson, E. C.; O'Keefe, M. A. Atomic resolution of lithium ions in $LiCoO_2$. *Nat. Mater.* **2003**, *2*, 464–467.

[48] Wolverton, C.; Zunger, A. First-principles prediction of vacancy order-disorder and intercalation battery voltages in Li_xCoO_2. *Phys. Rev. Lett.* **1998**, *81*, 606–609.